ADVANCED MATERIALS
www.advmat.de

Optically Pumped and Electrically Switchable Microlaser Array Based on Elliptic Deformation and *Q*-Attenuation of Organic Droplet Oscillators

*Masato Kato, Junnosuke Miyagawa, Shun-ichiro Noguchi, Naoki Takada, Soumei Baba, Satoshi Someya, Ankit Kumar Singh, Jer-Shing Huang, Yohei Yamamoto, and Hiroshi Yamagishi**

Conventional laser panel displays are developed through the mass integration of electrically pumped lasers or through the incorporation of a beam steering system with an array of optically pumped lasers. Here a novel configuration of a laser panel display consisting of a non-steered pumping beam and an array of electrically *Q*-switchable lasers is reported. The laser oscillator consists of a robust, self-standing, and deformable minute droplet that emits laser through Whispering-Gallery Mode resonance when optically pumped. The laser oscillation is electrically switchable during optical pumping by applying a vertical electric field to the droplet. Electromagnetic and fluid dynamics simulations reveal the deformation of the droplet into a prolate spheroid under the electric field and associated attenuation of quality factor (*Q*-factor), leading to the halt of the laser oscillation. A 2 × 3 array of droplets is fabricated by inkjet printing as a prototype of a laser panel display, and it successfully achieves the pixel-selective switching of the oscillation.

1. Introduction

The implementation of laser emitters as alternatives to conventional light sources is an emerging trend across various fields of optical engineering.[1,2] One promising application is a laser panel display that has been pursued for decades with an aim to renovate the existing panel displays made of light-emitting diodes (LEDs) and liquid crystals (**Figure 1a**).[3–5] While laser projectors consist of a handful of lasers, laser panel displays consist of an array of millions of laser oscillators that are switchable individually by electric signals.[6,7] The device configuration resembles that of conventional LED displays, but the mechanical assembly of the laser panel displays is

M. Kato, J. Miyagawa, S.-i Noguchi, Y. Yamamoto, H. Yamagishi
Department of Materials Science
Institute of Pure and Applied Sciences
and Tsukuba Research Center for Energy Materials Science (TREMS)
University of Tsukuba 1-1-1 Tennodai
Tsukuba, Ibaraki 305–8573, Japan
E-mail: yamagishi.hiroshi.ff@u.tsukuba.ac.jp

N. Takada, S. Baba
Research Institute for Energy Conservation
National Institute of Advanced Industrial Science and Technology (AIST)
Tsukuba, Ibaraki 305–8564, Japan

S. Someya
Department of Mechanical Engineering
Tokyo Denki University, Senjyu Asahicho
Adachiku, Tokyo 120–8551, Japan

A. K. Singh, J.-S. Huang
Research Department of Nanooptics
Leibniz Institute of Photonic Technology
Albert-Einstein Strasse 9, D-07745 Jena, Thuringia, Germany

A. K. Singh
Photonics Research Group
INTEC-department
Ghent University-IMEC, and Center for Nano- and Biophotonics
(NB-Photonics), Ghent University
Technologiepark-Zwijnaarde 126, Ghent B-9052, Belgium

J.-S. Huang
Institute of Physical Chemistry and Abbe Center of Photonics
Friedrich Schiller University Jena
D-07737 Jena, Thuringia, Germany

J.-S. Huang
Research Center for Applied Sciences
Academia Sinica
128 Sec. 2, Academia Road, Nankang District, Taipei 11529, Taiwan

J.-S. Huang
Department of Electrophysics
National Yang Ming Chiao Tung University
1001 University Road, Hsinchu 30010, Taiwan

The ORCID identification number(s) for the author(s) of this article can be found under https://doi.org/10.1002/adma.202413793

DOI: 10.1002/adma.202413793

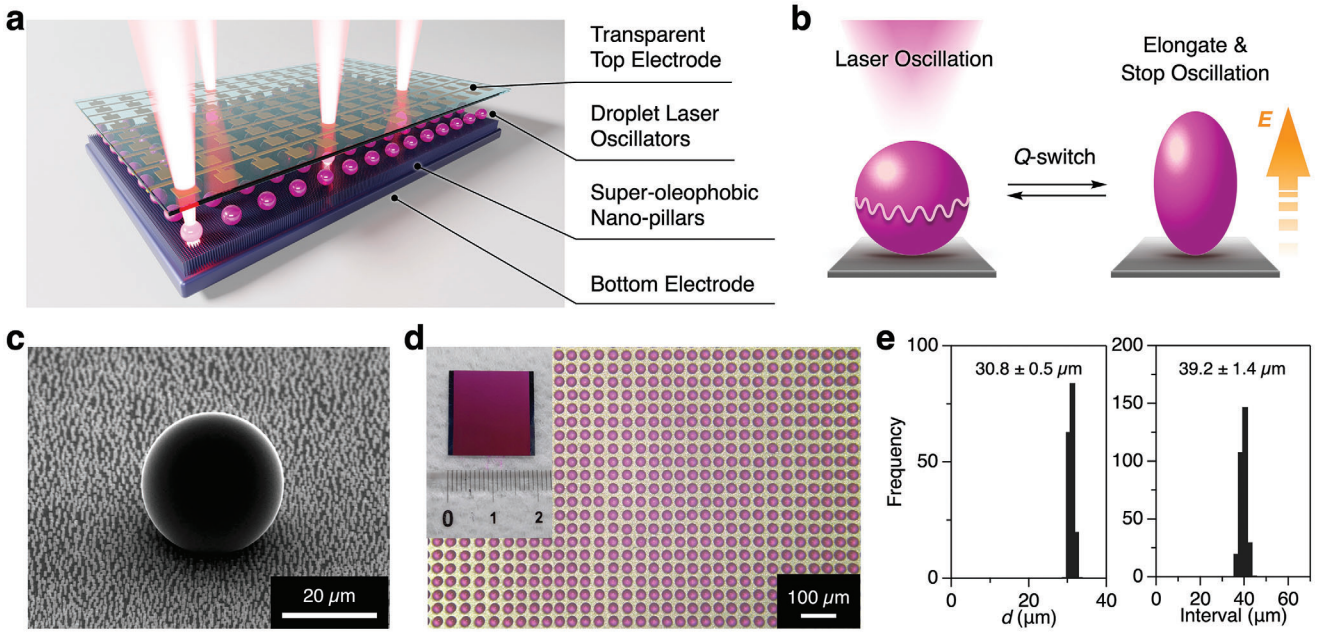

Figure 1. a) A schematic representation of a flat laser display. b) Schematic representations of a self-standing droplet oscillator that attenuates its *Q*-factor upon elongation induced by an external electric field. c) A scanning electron microscopic image of the self-standing droplet. d) An array of self-standing droplets. The inset shows the unmagnified image. e) Histograms of the diameter (*d*, left, $n = 167$) and interval (right, $n = 306$) of the droplets.

far more difficult because of the complexity and cost of building the dense array of blue, green, and red laser oscillators.[8,9] Typical edge-emitting diode lasers, with longitudinal dimensions ranging from several tens to hundreds of micrometers, are much larger than micro-LEDs and are too bulky for integration into an array.[9] Vertical-cavity surface-emitting lasers (VCSELs) are much smaller in footprint and can be developed on a flat substrate to form an array,[10–13] but VCSELs are currently inapplicable to full-color imaging due to the challenges in altering the active material and resonance frequency for each pixel.[14–16] Consequently, existing arrays of laser emitters are monochromatic and feature small pixel density.

The integration of optically pumped organic laser oscillators is an emerging strategy for manufacturing laser panel displays.[17,18] The organic oscillators are minute and can be assembled on a large scale using solution processes or inkjet printing. The pixels are pumped individually by an excitation beam, generating images and motion pictures when the scanning speed of the excitation beam is sufficiently fast. A 44 × 44 array of organic lasers has been previously reported, successfully showing vivid and full-color images.[19] However, these organic lasers are unsuitable for forming a thin and flat device because the beam steering mirrors must be fixed above or beneath the panel at a certain interval, which is hardly miniaturized or flattened. Additionally, the limited steering speed and refresh rate hinder their implementation in displays.

Liquid droplet lasers offer an alternative to the solid counterparts because of their excellent processability but their integration into arrays remains a significant challenge.[20] The droplet lasers reported so far have typically been manufactured by injecting droplets into an immiscible mother liquid and suspending them using optical tweezers, which is not suitable for array devices. While some droplet lasers have been deposited on a substrate and operated in the atmosphere, most of them were only temporarily stable due to morphological and optical instabilities.

We recently reported a highly deformable minute laser oscillator composed of an organic droplet.[21] The micro-droplet was composed of 1-ethyl-3-methylimidazolium tetrafluoroborate ($EMIBF_4$) featuring significantly low volatility and high surface tension. The low volatility effectively suppresses the evaporation of the liquid and ensures the morphological stability of the droplet under atmospheric conditions. Among commercially available ionic liquids, $EMIBF_4$ exhibits a relatively high surface tension, which enhances the contact angle of the droplet and contributes to the formation of a nearly spherical morphology. The droplet was self-standing on a substrate and exhibited exceptional chemical and physical robustness. It maintained its position, morphology, and optical performance with negligible changes even after several months of incubation in an ambient atmosphere without any sealing. The stability is substantially superior to conventional droplets, which typically survive only temporarily even in sealed chambers. The lasing threshold of the organic droplet was comparable to the best optically pumped organic lasers reported to date, including solid-state ones. We also discovered that the droplet was fluidic and deformed easily in response to air convection. The deformed droplet featured elongated optical path lengths and induced a peak shift in the laser emission.

These observations led us to hypothesize that a much stronger external force and associated substantial morphological

deformation could attenuate the qality factor (*Q*-factor) of the droplet and halt its laser oscillation even under optical pumping. Additionally, we surmised that the deformation of a liquid droplet could be achieved not only by applying pneumatic force but also by applying an electric field according to the theory of electrodynamic droplet deformation,[22–25] suggesting the possibility of electric *Q*-switching of the laser oscillation in the droplets (Figure 1b).

Based on this concept, here we present an organic laser display using optical pumping and electric *Q*-switching. The laser oscillator comprises a micrometer-sized spherical droplet of organic ionic liquid containing an organic laser dye as the gain material. The droplets were cast using an inkjet printer with high spatial precision and on a large scale onto a bottom electrode that was decorated with superoleophobic silicon nano-pillars to make the droplet spherical. The droplets were then sandwiched with a transparent top electrode, which enabled the application of a vertical electric field as well as the transmission of excitation and emission light. The droplet emitted laser upon strong photoexcitation while it ceased laser oscillation when a strong electric field was applied even upon optical pumping. Angle-dependent observations of the emission spectra, along with the electromagnetic and fluid dynamics simulations, revealed that the droplet transformed into a prolate spheroid under an electric field, leading to the attenuation of the *Q*-factor. To demonstrate the applicability of the *Q*-switchable droplet lasers for flat laser displays, we arranged the droplets into a 2 × 3 array and successfully switched the pixels independently by applying voltage.

2. Results and Discussion

2.1. Droplet Lasers and Electric Device

A laser pixel was composed of a bottom silicon (Si) electrode, a droplet laser oscillator, and a transparent top electrode (Figure 1a). The bottom Si electrode was fully covered with nano-pillars that provided superoleophobic support to maintain the droplet's spherical morphology (Figure 1c). The pillars were developed following the authors' previous report using the Bosch process (Figure S1, Supporting Information).[26] Typically, a thin layer of gold with a thickness of 10 nm was sputtered onto the bottom Si substrate and was converted into sub-micrometer-scale hemispherical dots by thermal annealing at 800 °C for 2 h. The substrate was subsequently subjected to dry etching, during which the gold hemispheres served as a mask, yielding nano-pillars with an average diameter of 420 nm, height of 2.1 µm, and spacing of 800 nm. The gold dots at the top of the pillars were removed with AURUM-302, and the complete removal of Au was confirmed by elemental mapping (Figure S2, Supporting Information). The pillars were highly oleophobic and substantially improved the contact angle from 33 to 155° when casting a droplet of $EMIBF_4$, while the contact angle was dependent on the surface tension of the liquid. For instance, a droplet of 1-butyl-3-methylimidazolium bis(trifluoromethanesulfonyl)imide featuring a relatively small surface tension (33 mN m^{-1}) showed a contact angle of 116° (Figure 1c; Figure S3, Supporting Information).[27]

An inkjet printer specialized for viscous liquids (Microjet model LaboJet-600) was employed to deposit droplets of $EMIBF_4$. An aliquot of $EMIBF_4$ doped with acid red 52 (AR52) for better visibility was loaded into the printer head and dispensed onto the substrate as spherical droplets with an average diameter of 30.8 µm (Figure 1e). Despite their large contact angle and small contact area, the droplets adhered tightly to the pillars and showed no slipping or spreading even under severe agitation. The droplets were deposited over a large area (20 × 20 mm) at high density (650 droplets per 1 mm^2, Figure 1d) with a spatial precision of 1.4 µm (Figure 1e). Given that three droplets constitute one full-color pixel, the array density shown in Figure 1d is comparable to that of a commercial 40-inch 8K monitor featuring 220 pixels per inch. After inkjet printing, a glass plate coated with indium tin oxide (ITO) on the bottom side was positioned 100 µm above the bottom Si substrate, which was utilized in the latter experiments to apply an electric field to the droplets with electrical flux lines orthogonal to the substrate. An insulating spacer with a thickness of 100 µm was inserted between the electrodes to maintain the gap (Figure S4, Supporting Information).

The photoluminescence (PL) spectra from a single droplet on the substrate were measured with the optical setup illustrated in **Figures** 2a and S5 (Supporting Information). Hereafter, the droplet of $EMIBF_4$ was doped, instead of AR52, with 2-[4-(dimethylamino)styryl]-1-methylpyridinium iodide (DASPI, 5.0 mg mL^{-1}) as a laser dye, together with β-cyclodextrin (CD, 16 mg mL^{-1}) as an anti-photobleaching reagent.[28] The droplet was excited with fs-laser pulses ($\Delta = 80$ fs, $\lambda = 460$ nm, $f = 1$ kHz, spot size = 100 µm), and the emission was collected using an optical fiber (core diameter = 355 µm, N.A. = 0.22) set on a rotatable table to obtain angle-resolved PL spectra (Figure S5, Supporting Information). The angle of the optical fiber is denoted as θ, and its origin is set on the normal of the substrate.

Figure 2b shows a PL spectrum obtained at $\theta = 30°$ without applying any electric field. The PL profiles exhibited periodic sharp peaks attributed to transverse electric and magnetic (TE and TM) modes of Whispering Gallery Mode (WGM) optical resonance (Figure S6, Supporting Information), which were identified as laser emission based on peak narrowing and emission amplification with a threshold power (P_{th}) of 109 µJ cm^{-2} (Figure 2c). The average P_{th} of the three spheres was 138 µJ cm^{-2}. In contrast, $EMIBF_4$ droplets with a smaller contact angle (111°) did not radiate laser even upon pumping with P of 25 mJ cm^{-2}, demonstrating the advantage of a spherical droplet with a large contact angle as the laser oscillator (Figure S7, Supporting Information). The laser emission was observed isotropically within a θ range of 20–70° (Figure S8, Supporting Information), which is characteristic of spherical WGM resonators. Isotropic radiation is generally disadvantageous for typical laser applications but is advantageous for display applications since the emission is visible from wide viewing angles.[29] The droplet emitted multimode lasers, which is less ideal for typical laser applications, but the spectral broadness is satisfactory for display applications (Figure S9, Supporting Information).[30,31] We also found that the droplets radiated laser even when a ns-laser was used as the excitation source, although we found that the ns-laser caused more intense photobleaching of the dyes (Figure S10, Supporting Information).

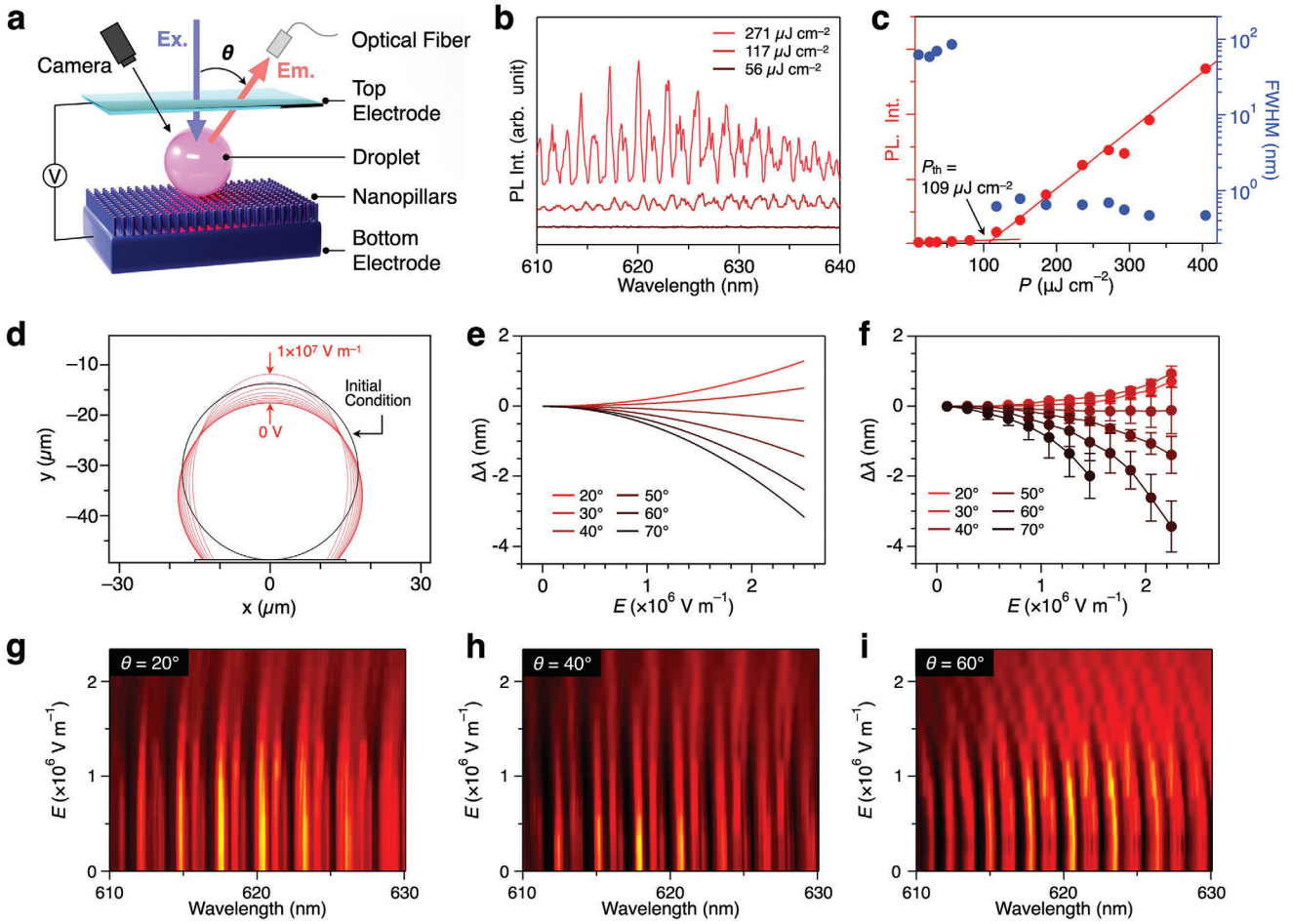

Figure 2. a) A schematic representation of a laser pixel and the optical setup. b) Photoluminescence (PL) spectra of the droplet upon photoexcitation with P of 56, 117, and 271 μJ cm^{-2}. c) Plots of the PL intensities (red dots) and full width at half maxima of a peak at 620.2 nm (blue dots). d) Simulated morphologies of a droplet under a static electric field with E ranging from 0 to 1×10^7 V m^{-1} (red curves). The black curve shows the morphology of the droplet in the initial condition. e) Mathematically calculated spectral shifts of the WGM resonance in an elongated droplet upon increasing E from 0 to 2.5×10^6 V m^{-1} and upon sweeping θ from 20 to 70°. f) Experimentally observed spectral shifts of the laser peaks emitted from a droplet upon increasing E from 0 to 2.3×10^6 V m^{-1} and upon sweeping θ from 20 to 70°. ($n = 3$) g–i) Experimentally observed PL spectra of a droplet observed at $\theta = 20$, 40, and 60° upon increasing E from 0 to 2.3×10^6 V m^{-1}.

2.2. Deformation of Droplets Under Electric Fields

Theoretically, a dielectric spherical droplet deforms under a static electric field into a prolate spheroid with its longer axis parallel to the electric flux line (Figure 1b). The degree of deformation (D), defined as the ratio between the longer and the shorter axes, depends on the diameter (d) of the droplet, its surface tension (γ), and the strength of the static electric field (E) as follows:

$$D = C \frac{d}{\gamma} E^2 \tag{1}$$

where C is a parameter derived from the conductivity, permittivity, and viscosity of the droplet and the surrounding medium (see Methods for details). For example, with $d = 30$ μm, $\gamma = 50$ mN m^{-1}, and $E = 2 \times 10^6$ V m^{-1}, the droplet elongates 0.24 μm along the electric field, while the diameter at the equator shrinks by 0.12 μm. Since the optical resonance wavelength is proportional to the optical path length, the elongation of the droplet leads to a peak shift of the WGM resonance, which is dependent on θ. We calculated the theoretical peak shifts of the WGM resonance (see Methods) and found that, at smaller θ, the peak shift is directed toward a longer wavelength region, while the shift is reversed at higher θ with a threshold θ (θ_{th}) between 30 and 40° (Figure 2e).

In reality, the droplet was not a perfect sphere but a hemisphere due to contact with the pillars. To visualize the hemispherical morphology of the droplet sitting on the pillars, we conducted computational fluid dynamics simulations and found that the change in D as a function of E closely matched the predictions given by Equation (1) (Figure 2d; Figure S11, Supporting Information). We also computed the spectral shift of resonance peaks inside a prolate spheroid using the finite-difference time-domain method (FDTD, Figure S12, Supporting Information), assuming the D of the spheroid varies with E as described by Equation (1). As illustrated in Figures S13 and S14 (Supporting

Information), the resonance wavelength shifted toward longer wavelengths at smaller θ as increasing E. Conversely, the direction of peak shift reversed toward shorter wavelengths at $\theta > 50°$ (details of the simulation method, results, and discussions are written in the "FDTD simulation method for microsphere" section in Methods).

We experimentally observed consistent spectral responses from the droplet. We utilized the setup illustrated in Figure 2a and applied an electric field to the droplet with a sawtooth waveform, where E increased linearly from 0 to 2.3×10^6 V m^{-1} in 6 sec. In the course of applying voltage, the droplet was continuously pumped with the fs-laser with P of 340 μJ cm^{-2}, and the emission was collected at every 0.5 sec. When θ was 20°, the wavelengths of the laser peaks shifted slightly toward longer wavelengths with increasing E, and the peak shift became more pronounced at larger E (Figure 2g). A similar trend was observed at $\theta = 30°$ (Figure S13b, Supporting Information). At 40°, we observed a distinct spectral response (Figure 2h), where the spectral changes were negligible, and all laser peaks remained nearly static regardless of E. At even higher θ, the peak shift reversed toward shorter wavelengths (Figure 2I; Figure S13, Supporting Information). The parabolic curves λ plotted against E in Figure 2f and the reversal of curvature were consistent with the theoretical curves (Figure 2e) although the curvature reversal happened at slightly larger θ. The discrepancy in θ_{th} between theoretical predictions and experimental observations was ≈5°, which was attributed to the contact between the droplet and the substrate that deformed the droplet into a spherical cap rather than a perfect prolate spheroid.

As additional support for the elongation of the droplet, we made a log–log plot of the peak shifts for every θ (Figure S15, Supporting Information). The plots were nearly linear with an average slope of 2.12, meaning that the peak shifts in Figure 2f are a quadratic function of E. Considering that the peak shift is generally in a linear relationship with D as long as the shift is sufficiently small (the detailed equation is written in Methods),[32] the plots in Figure S15 (Supporting Information) indicated that D was also a quadratic function of E as expected from Equation (1). These results further corroborate the elongation of the droplet into a prolate spheroid under an electric field.

2.3. Electric Switching of the Laser Oscillation

Concomitant with the spectral shift, the deformation of the droplet impacted the light confinement efficiency. It is known that elliptical modes experience enhanced light leakage and a lower Q-factor compared to those in a perfect circle due to chaotic resonance.[33,34] In addition to this effect, we assumed that the Q-factor of a 3D elliptical spheroid is further attenuated due to the tilted edge. The tangential plane at the circumference in a cross-section diagonal to the equator of the prolate spheroid is not perpendicular to the cross-section (Figure S16a, Supporting Information), leading to deviation of the light path. To validate this prediction, we conducted computational simulations using FDTD methods to calculate the light confinement efficiency (Figure S16b, Supporting Information) and found that the Q-factor of a circular disk decreased with increasing tilt of the tangential plane. Consistent with these results, our previous work on optically elliptical spheroids showed that the electromagnetic field strength at diagonal and vertical cross-sections was attenuated upon elongation.[35,36]

We analyzed the changes in Q-factor in Figure 2g–I and Figure S13 (Supporting Information) and found a decline in Q-factor from 2.28×10^3 to 1.24×10^3 as E increased from 0 to 2.3×10^6 V m^{-1} at $\theta = 20°$ (**Figure 3a**). Concomitantly, the lasing threshold increased by 45 μJ cm^{-2} (ΔP_{th}, Figure 3b). These results were consistent with the above-described predictions and simulations. We also found that the decrease in Q-factor and the elevation of ΔP_{th} were mitigated at larger θ. The small changes in Q-factor and ΔP_{th} at larger θ are reasonable because the ellipticity of the light path and the tilt of the tangential plane are not as severe as those at smaller θ.

In addition, we analyzed the integrated photocounts of emissions generated through stimulated and spontaneous pathways, respectively, in a wavelength range from 610 to 625 nm and plotted them as a function of E (Figure 3c). Initially, the intensity of laser emission predominated over spontaneous emission at $E = 0$ V m^{-1}, but their relative populations reversed at higher E. As is well known, the rate of stimulated emission is proportional to the electric field strength in the medium,[37,38] indicating that the presence of lossy elliptical modes reduced the probability of the stimulated radiation process. In contrast, the rate of spontaneous emission is independent of the electric field strength and becomes dominant in a highly deformed droplet, which reasonably explains the intensity reversal observed with the droplet at higher E.

We then observed the Q-switching behavior. With the setup illustrated in Figure 2a, we continuously irradiated the droplet with the excitation fs-laser and applied square electric waveforms to induce switching of the laser oscillation in the droplet. We alternated E from 0 to 2.0×10^6 V m^{-1} repeatedly and succeeded in switching the laser oscillation at repetition rates of 0.025 and 1 Hz (Figure 3d,e). We observed negligible changes in lasing performance over 60 cycles, as evidenced by the emission spectra (Figure S17, Supporting Information). Electric switching was successfully demonstrated with three different devices, confirming the reproducibility of the device setup (Figure S18, Supporting Information). Moreover, the Q-switching was visually detectable. Emission from the single droplet was observed using an optical microscope that was positioned diagonally to the substrate (Figure S5, Supporting Information). A bandpass filter (λ_{center} = 630 nm, FWHM = 10 nm) was additionally inserted to eliminate spontaneous emission. The red emission localized at the periphery of the droplet significantly darkened upon the application of an electric field of 2.5×10^6 V m^{-1} (Figure S19 and Video S1, Supporting Information). The on–off ratio of the laser emission was enhanced by introducing a saturable absorber layer on the top electrode.[39,40] The absorber layer was created by spin-coating a binary mixture of water and ethanol (1/1 v/v) containing polyvinyl alcohol (50 mg mL^{-1}) and 3,3′-diethylthiadicarbocyanine iodide (DTDCI, 2.3 mg mL^{-1}). With the absorber layer in place, spontaneous emission from the droplet under an electric field was largely attenuated as shown in Figure 3f,g and Video S2 (Supporting Information). We attributed the enhanced contrast to the reduced

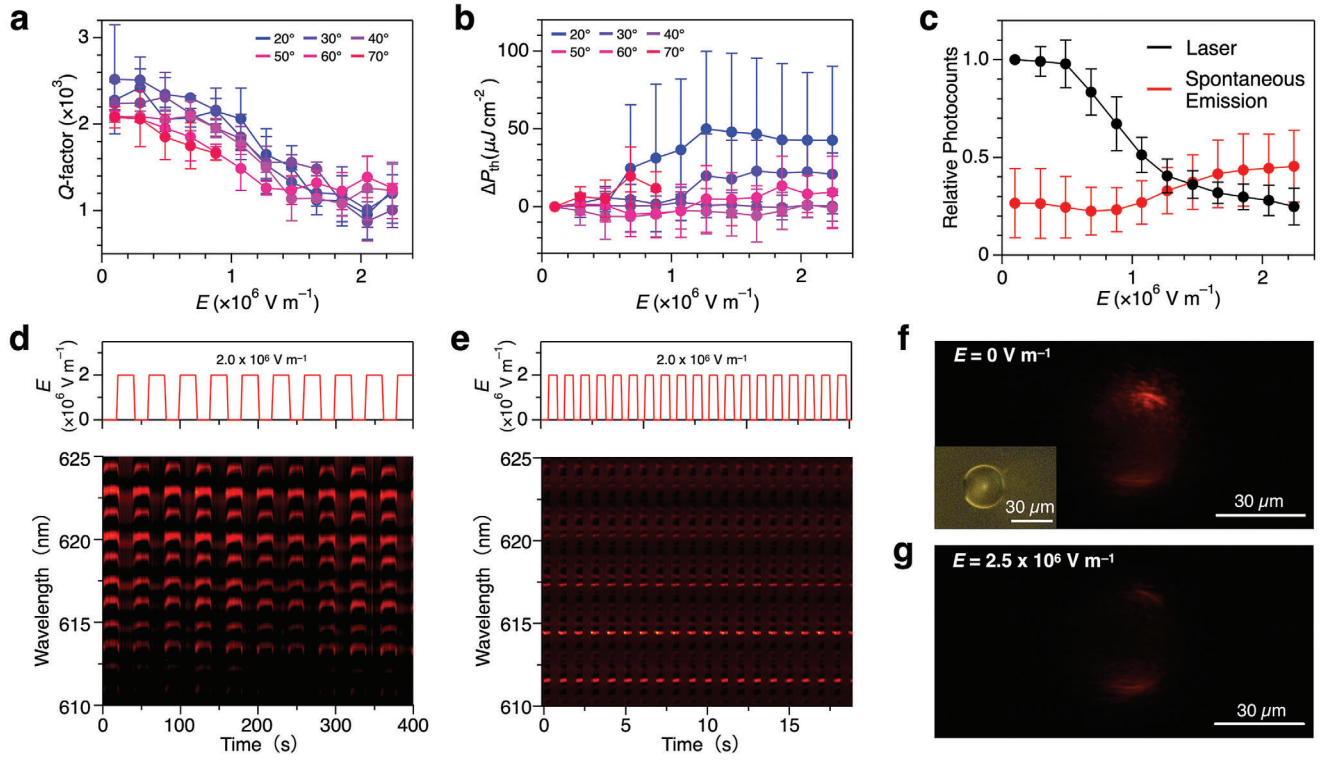

Figure 3. a,b) Plots of Q-factor (a) and ΔP_{th} (b) of a droplet upon increasing E from 0 to 2.3 × 10^6 V m^{-1} and sweeping θ from 20 to 70°. (n = 3) c) Plots of the integrated PL intensities of laser peaks (black dots) and broad spontaneous emission band (red dots) observed at θ = 30°. (n = 3) The photocounts are normalized with respect to that of laser peaks observed at E = 0 V m^{-1}. d,e) PL spectra of a droplet applied with periodically oscillating E at a repetition rate of 0.025 (d) and 1 Hz (e), respectively. The upper panels show E applied to the droplets. f,g) Microscopic images of a droplet upon photoexcitation with E of 0 (f) and 2.5 × 10^6 V m^{-1} (g), respectively. The inset shows a bright field image.

absorption of laser emission by the absorber layer. As written above, the switching contrast of the device without the absorber layer decreased due to persistent spontaneous emission, which occurred regardless of the applied electric field. The absorber layer suppressed the spontaneous emission, while the layer was less effective in attenuating the laser emission due to absorption saturation.

2.4. Array of Laser Oscillators

As a prototype of a laser display, droplets were deposited onto the substrate to form a 2 × 3 array and sandwiched with a transparent top panel patterned with an array of small ITO pads for applying electric fields to each droplet (**Figure** 4a,b). The droplets were spaced at intervals of 250 μm (Figure 4c), and the electrode pads were connected to a DC power source (Figure S20, Supporting Information). An excitation laser (λ = 355 nm, Δ = 1.4 ns, f = 1 kHz) was directed onto each droplet, and the PL spectra were observed at E = 0 and 8 × 10^6 V m^{-1}, respectively. While the droplets emitted laser when E was off (Figure 4d), all the droplets ceased to emit laser upon applying voltage. The laser switching could be performed individually for all 6 droplets. Subsequently, we tried expanding the spot size of the excitation laser to excite the entire array simultaneously. However, the trial was unsuccessful so far due to the inhomogeneous power density of the laser spot. We are also working to scale up the array, but this effort is currently limited by the device assembly process and the yield ratio of the droplet lasers (Figure S21, Supporting Information).

3. Conclusion

A novel electrically switchable droplet laser and its array were demonstrated. The droplets were deposited by inkjet printing with high precision and scalability, and its laser oscillation was switchable by applying an electric field using a pair of electrodes. Fluidic dynamics and electromagnetic simulations revealed the deformation of the droplet and the concomitant Q-attenuation. The novel device configuration for laser switching presented here will contribute to future advancements in laser displays, although the pumping energy and the lifetime of the laser dyes must be improved beforehand. In addition, the liquid nature of the droplet offers significant potential for next-generation optoelectronic devices since the droplets can be integrated into existing organic electronics that are characterized by flexibility, adaptability, and biocompatibility.[41–44] While the laser display described here still remains bulky and thick due to the photoexcitation setup, future advancements in waveguiding technologies[45] hold promise for miniaturizing and flattening both the light source and the optical path.

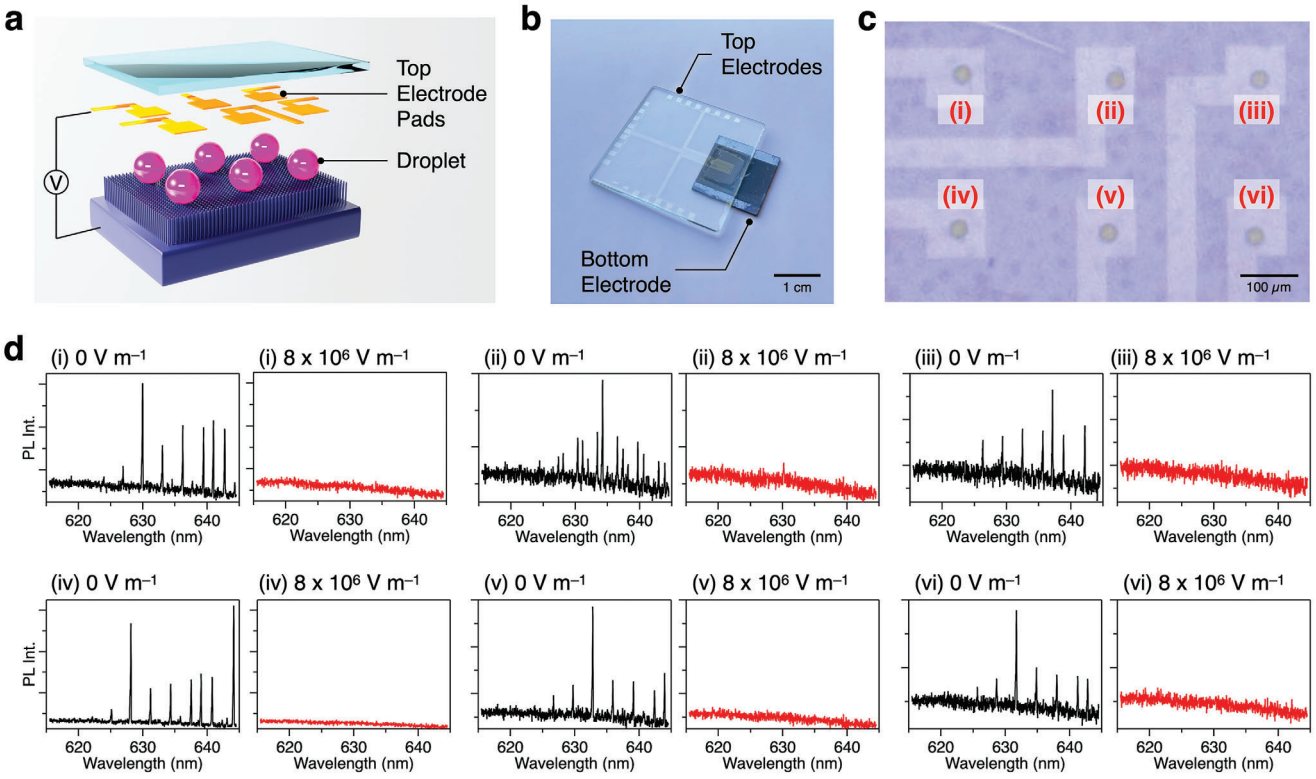

Figure 4. a) Schematic representation of an array of laser pixels. b,c) Unmagnified (b) and magnified (c) photographs of the laser array device. The Roman numbers indexed to the individual droplets correspond to the spectra in Figure 4d. d) PL spectra of the droplets (i) to (vi) observed under $E = 0$ (black) and 8×10^6 V m^{-1} (red).

4. Experimental Section

Materials and Methods: P-doped Si wafer with a 200 nm-thick SiO_2 layer was purchased from Fruuchi Chemical. Other chemicals and reagents were purchased from Sigma-Aldrich, TCI, Kanto Chemical, and Merck. Unless otherwise noted, all reagents and solvents were used as received. Scanning electron microscope (SEM) images were taken on a Hitachi model S-3700N SEM operating at 15 kV. The contact angle was measured based on optical microscopic images viewed from the horizontal direction with a KEYENCE model VHX-S50 free-angle observation system and analyzed with free software ©2019 Kei Ono.

Fabrication of the Pillared Substrate, Droplet Oscillators, and Electric Devices: Onto a 4-inch P-doped Si substrate covered with a 200 nm-thick SiO_2 layer, a thin layer of gold with a thickness of 10 nm was sputtered using Shibaura Mechatronics Corporation model CFS-4EP-LL. The Si substrate was then baked under N_2 at 800 °C for 2 h by using a muffle furnace (Yamato Scientific Co., Ltd. Model, FP100) to convert the gold layer into sub-micrometer-scale hemispherical dots. The substrate was subsequently subjected to plasma etching (Samco Model, RIE-101iPHS-L), where the gold dots worked as a resist. First, the SiO_2 layer was etched using CHF_3 gas. The underlying Si substrate was then developed by the Bosch process using SF_6 and C_4F_8 for etching and passivation steps, respectively, yielding nano-pillars. The gold dots at the top of the pillars were removed with AURUM-302.

The droplets were deposited onto the substrate using an inkjet printer (MICROJET model, LaboJet-600) equipped with an inkjet head specialized for viscous liquid (IJHE-30).

The top electrode pads were developed on a glass plate ($30 \times 30 \times 1$ mm) using photolithography and sputtering. First, an aliquot of hexamethyldisilazane (HMDS) was spin-coated on the plate and air-dried. A resist (AZ5142E) was spin-coated onto the plate and was baked at 110 °C for 2 min. Subsequently, the resist was subjected to maskless photolithography (Heidelberg Instruments, μPG501). After development using NMD-3, the ITO layer was deposited onto the whole substrate using Shibaura Mechatronics Corporation model CFS-4EP-LL. The resist layer beneath the ITO was then lifted off using acetone, yielding patterned electrode pads.

The top electrode substrate was fixed manually on the bottom substrate using a double side tape with a thickness of 100 or 50 μm as the spacer. The top and bottom electrodes were then wired to the electric circuits, and the electricity was supplied from a lithium polymer battery (Figure S20, Supporting Information). The voltage was amplified using a handmade DC-to-DC boost converter to reach a maximum output of 400 V, corresponding to an electric field of 8.0 MV m^{-1}, given the 50 μm gap between the top and bottom electrodes.

The saturable absorber layer was created on a thin glass substrate ($18 \times 18 \times 0.15$ mm) by spin-coating a binary mixture of water and ethanol (1/1 v/v) containing polyvinyl alcohol (50 mg mL^{-1}) and 3,3′-diethylthiadicarbocyanine iodide (DTDCI, 2.3 mg mL^{-1}), followed by drying under the atmosphere. The glass plate with the saturable absorber layer was then attached to the top electrode substrate using double-sided tape with a thickness of 100 μm.

Microscopic Photoluminescence Spectroscopy (μ-PL): Microscopic photoluminescence (μ-PL, Figure S5, Supporting Information) spectroscopy was conducted by using, as the pumping light, a femtosecond (fs) light source (Spectra-Physics Inc. model, Solstice Ace70F, f: 1 kHz, Δ: 70 fs, λ: 800 nm) and a collinear optical parametric amplifier (Spectra-Physics Inc. model, TPR-TOPAS/NMW-UV1). The pumping laser is irradiated perpendicularly to the substrate. The emission was collected with a bundled optical fiber set on a rotatable stage and was transferred to a spectrometer (Teledyne Princeton Instruments model, HRS-300MS-NI-F, grating: 1800 grooves mm^{-1} and PIXIS-256E-HF). An objective lens is set diagonal to

the substrate (Olympus, Plan Semi-Apochromat-LMPLFLN, 20x, 0.4 NA) for the visual observation of the droplets. Microscopic photoluminescence (μ-PL) spectroscopy with a ns excitation laser (CryLaS model FISS355-Q4, $\lambda = 355$ nm, Δ: 1.4 ns, *f*: 1 kHz, laser spot diameter 300 μm) was conducted on an optical microscope (Nikon model Eclipse LD100D) equipped with an objective lens (Nikon, LU Plan Fluor, 20x, 0.45 NA) and a spectrometer (Lambda Vision model LV-MC3/T, grating: 1800 grooves mm^{-1}, optical resolution: 0.01 nm, Figure S20, Supporting Information).

Statistical Analysis: Normalization was conducted for the data utilized for Figure 3c by dividing the observed integrated photocounts with that attributed to the laser peaks at $E = 0$ V. The data was presented in the form of mean ± standard deviation. The error bars represent the standard deviation. The sample size is shown in each figure legend. The mean and standard deviation are calculated using Microsoft Excel.

Taylor-Melcher Leaky Dielectric Model: A classical Taylor–Melcher leaky dielectric model (LDM) was used for the prediction of droplet elongation under a static electric field. Given a droplet is floating in a medium, the deformation ratio *D* of the droplet is defined as follows,

$$D = \frac{a-b}{a+b} \tag{2}$$

where a and b represent the longer and shorter axis of the prolate spheroid. Based on the LDM model, D is provided as follows,

$$D = \frac{9}{16}\phi_0 \frac{\epsilon_d r_d E^2}{\gamma} \tag{3}$$

$$\phi_0 = \frac{1}{(R+2)^2}\left[S\left(R^2+1\right) - 2 + (SR-1)\,\Omega\right] \tag{4}$$

$$\Omega = 3\frac{2M+3}{5M+5} \tag{5}$$

$$S = \frac{\epsilon_m}{\epsilon_d} \tag{6}$$

$$M = \frac{\mu_m}{\mu_d} \tag{7}$$

$$R = \frac{\sigma_d}{\sigma_m} \tag{8}$$

where r_d, and γ are radius and surface tension of the droplet, *E* is the electric field applied, ϵ_m, μm, and σ_m are permittivity, permeability, and conductivity of the media, and ϵ_d, μ_d, and σ_d are permittivity, permeability, and conductivity of the droplet.

The circumference (*L*) of an elliptical cross-section of a prolate spheroid is, approximately, provided as a function of the tilt angle of the cross-section (θ) against the meridian as follows:

$$L = \pi\left(r_\theta + b\right)\left(1 + \frac{3\left(\frac{r_\theta - b}{r_\theta + b}\right)^2}{10 + \sqrt{4 - 3\left(\frac{r_\theta - b}{r_\theta + b}\right)^2}}\right) \tag{9}$$

$$\alpha = \frac{1+D}{1-D} = \frac{a}{b} \tag{10}$$

$$b = 2r_d \times \alpha^{-\frac{1}{3}} \tag{11}$$

$$a = 2r_d \times \alpha^{\frac{2}{3}} \tag{12}$$

$$r_\theta = \sqrt{\left(\frac{a}{2}\cos\theta\right)^2 + \left(\frac{b}{2}\sin\theta\right)^2} \tag{13}$$

$$\frac{\Delta\lambda}{\lambda} = \frac{L - 2\pi r_d}{2\pi r_d} \tag{14}$$

where r_θ is the length of the longer axis of the ellipse of the cross-section, α is the ratio between *a* and *b*, λ is the resonance wavelength, and $\Delta\lambda$ is the peak shift.

Fluid Dynamics Simulations: Fluid dynamics simulations were conducted using the commercial software COMSOL Multiphysics, which adopts the finite element method (FEM) as a numerical solution scheme for visualizing the morphology of an organic droplet on a solid surface in a gas under static electric field. A set of two-phase fluid mass and momentum conservation equations with the Cahn-Hilliard (CH) interface advection equation in the phase-field method (PFM)[46,47] and the electrostatic equations[48] in steady state were numerically solved by FEM. Based on the free-energy theory, the PFM models an interface as a finite-volumetric transition zone, across which the physical properties vary steeply and continuously between different phases. The diffuse-interface regions retain their thickness to be constant due to diffusion flux, which is induced by chemical-potential gradient as the fluid system evolves toward an equilibrium state to minimize its free energy. The CH equation describes the time evolution of the spatial distribution of a continuous variable ϕ in the flow field. In the present simulations, the gas phase, liquid phase, and gas–liquid interface corresponded to the fluid regions with $\phi = -1$, $\phi = 1$, and $-1 < \phi < 1$, respectively. The representative interfacial positions were measured with a contour of $\phi = 0$ (Figure 2d). In this study, a 2D computational domain was set for the sake of simplicity because the 3D fluid dynamics simulations are computationally intensive and demanding. The 2D computational domain of 200 μm × 100 μm in the Cartesian coordinate system (*x*, *y*) was partitioned into 68 394 triangular mesh cells and surrounded by continuous outgoing boundaries on the left and right sides, and by nonslip-wall boundaries with static contact angle of the liquid phase $\theta_W = 121°$ on the top and bottom sides, respectively (Figure S11, Supporting Information). The contact angle was set based on the experimental observation of the droplet sitting on a SiO_2 pillar with a diameter and height of 30 and 1.2 μm, respectively. The wall-surface wettability to the two-phase fluid was considered through the wall boundary condition for ϕ, $\mathbf{n}_W \cdot \nabla\phi = -|\nabla\phi|\cos\theta_W$, where $\mathbf{n}_W$ is the unit vector to the wall surface, and the unit vector normal to the interface is $-\nabla\phi/|\nabla\phi|$.[49] In the initial condition, a circular-shaped droplet with a diameter of 35 μm was placed on a pedestal with a width of 30 μm and a height of 1.2 μm at the center of the bottom wall. The density, viscosity, relative permittivity, and conductivity of the gas phase were 1.18 kg m^{-3}, 1.82×10^{-5} Pa s, 1.0, and 1.0×10^{-14} S m^{-1} whereas those of the liquid phase were 1.29×10^3 kg m^{-3}, 3.75×10^{-2} Pa s, 12.9, and 1.41 S m^{-1} respectively.[50–53] The surface tension was set at 5.21×10^{-2} N m^{-1}.[54] In each case of the strengths of the static electric field applied between the top and bottom walls, the droplet shape reached a steady state.

FDTD Simulation Method for Microsphere: A 3D finite-difference time-domain (FDTD) simulation was set up to calculate the response of a microsphere (refractive index = 1.416 + 0.0004*i*) placed on a silicon substrate with a 200 nm-thick SiO_2 layer (Figure S12, Supporting Information). Perfectly matched layer boundaries were used to define the simulation region to avoid any nonphysical reflection of the electromagnetic waves by the boundaries. The mesh accuracy of the simulation was set to 2 to obtain accurate results within reasonable simulation time.

The WGMs were excited by three short-pulsed dipoles placed inside the sphere and polarized along the x, y, and z-axis, respectively. The dipoles were positioned 500 nm away from the surface of a sphere in the equatorial plane to effectively excite all the WGM modes. The fields were allowed to evolve, scatter, and eventually vanish over a simulation time of 3500 fs. Point monitors positioned at different angles between 0 and 90° at a distance of 100 nm outside the sphere were used to obtain the near-field spectrum at various angles. To avoid interference from the background field due to uncoupled dipole emission within the first 250 fs, the monitors were start-apodized for 250 fs with a width of 100 fs. Finally, the same model was used to simulate the ellipsoidal microsphere by tuning the radius of the sphere along different axes.

The results of FDTD simulations of the WGM microsphere are shown in Figures S12–S14 (Supporting Information), which shows the change in the WGM spectrum with applied voltage (ellipticity) as a function of the detection angle θ. While the trend of the spectral shift shows good agreement between simulated and experimental data, minor differences are observed. Possible reasons for the difference are as follows. First, the experimental spectra show "lasing" WGMs peaks. Therefore, they have a rather clean background because other WGM peaks that do not show lasing have comparably begligible intensity. This makes the spectral shift of the peaks clear. In contrast, in the simulated spectra, all WGM peaks are visible, no matter they show lasing or not. This makes the spectra crowded and the tracing of peak position complicated and difficult because the distortion of the cavity shape not only leads to shift but also splitting of the originally degenerated WGM peaks. Second, the geometry of the spheroid in the simulation might not be exactly the same as that in the experiment. For example, the contact angle/area of the ellipsoid in the simulation is solely decided by the volume and ellipticity of the particle (related to the electric voltage) while the actual shape of the microsphere may be slightly different due to the local electric field and local substrate condition. The third reason for the deviation between the experimental and FDTD spectrum can be the low accuracy of the mesh used for the simulation. Due to the large size of the particle, the mesh size cannot be too small. It needs to be carefully chosen such that the simulation time and the memory of each simulated job are within a reasonable range that can be handled and processed. Therefore, the optimal mesh is a cubical mesh of ≈20 nm side length. This can still be further improved by using more powerful hardware. Due to these reasons, the simulated and experimental results are not exactly the same. Nevertheless, the trend of spectral shift with respect to the applied voltage at various observation angles does match well between the simulation and experiment, verifying the model of shape distortion.

The Effect of Boundaries Orientation on the WGM Modes: FDTD Simulations of Microdisks: The WGM modes inside a uniformly excited spherical particle remain the same at all detection angles due to the spherical symmetry of the particle. However, when the particle is distorted to an elliptical shape, the symmetry is broken, and the emission spectrum of the particle becomes angle-dependent, i.e., the spectral position and the *Q*-factor of the resonant peaks in the spectrum depend on the observation angle θ.

This dependence can be attributed to the change in the particle's radius along the observation angle. Additionally, the inclination of the sphere boundary (Figure S16, Supporting Information), as experienced by the WGMs, changes upon the ellipticity and observation angle. This leads to ineffective total internal reflection at the boundary and thus reduces the *Q*-factor. This effect is particularly pronounced for WGMs orbiting along non-equatorial planes. Apart from the *Q*-factor reduction, a significant shift in the resonance position was also observed. This shift originates from the reduction in the effective area of the plane and, hence, the effective circumference of the mode inside the cylinder. Moreover, the non-orthogonal interface leads to more leakage of the modes due to non-ideal electromagnetic boundary conditions for transverse electric (TE) and transverse magnetic (TM) modes. It also breaks the mode degeneracy, leading to mode splitting, which appears as additional peaks at higher deformation angles (Figure S16, Supporting Information).[35]

The simulation settings for the microdisk particles were kept very similar to those for the sphere, with a few changes. The particles were assumed to be in a vacuum environment and designed such that the radius of the mode plane was always fixed at 15 µm and the height was 0.6 µm. The simulations were allowed to run until an auto-shutoff was triggered (shutoff threshold = 10^{-5}).

Supporting Information

Supporting Information is available from the Wiley Online Library or from the author.

Acknowledgements

This work was financially supported by CREST (JPMJCR20T4) and ACT-X (JPMJAX201J) from Japan Science and Technology Agency (JST), Grant-in-Aid for Scientific Research (B) (JP24K01306), Scientific Research (C) (JP20K04297), Transformative Research Areas (JP24H01693), Young Scientist (JP22K14656), Fund for the Promotion of Joint International Research (International Collaborative Research, 23KK0099) from Japan Society for the Promotion of Science (JSPS), DAAD-Tsukuba partnership program (No. 117235241) from University of Tsukuba. This work was supported by "Advanced Research Infrastructure for Materials and Nanotechnology in Japan (ARIM)" of the Ministry of Education, Culture, Sports, Science and Technology (MEXT, Grant Number JPMXP1222AT0083). J.-S.H. and A.K.S. acknowledge the support from DAAD (Projekt-ID: 57710865) and DFG (SFB 1375/2-C1, Project No.: 398816777 and HU 2626/5-1, Project No.: 445415315).

Conflict of Interest

The authors declare the following competing financial interest(s): M.K., J.M., Y.Y., and H. Y are listed as inventors on Japanese patent applications (No. 2022-128956 and 2023-015332).

Author Contributions

H.Y. and Y.Y. conceived the idea; M.K., J.M., S.N., and H.Y. designed and conducted the experiments; N.T., S.B., and S.S. conducted the fluid dynamics simulations; A.K.S. and J.-S.H designed and performed the FDTD simulations and interpreted the results; H.Y. and Y.Y. prepared the manuscript with the feedback from the other authors.

Data Availability Statement

The data that support the findings of this study are available from the corresponding author upon reasonable request.

Keywords

ionic liquid, laser display, microdroplet, printable laser, Q-switch

Received: September 13, 2024
Revised: November 15, 2024
Published online: December 17, 2024

[1] J. Liang, Y. L. Yan, Y. S. Zhao, *Acc. Mater. Res.* **2021**, *2*, 340.
[2] S. X. Li, L. Wang, N. Hirosaki, R. J. Xie, *Laser Photon. Rev.* **2018**, *12*, 1800173.
[3] J. Liang, K. Wang, Y. Du, C. Zhang, Y. Yan, Y. S. Zhao, *ACS Appl. Mater. Interfaces* **2022**, *14*, 1774.
[4] X. Zhan, F. F. Xu, Z. Zhou, Y. Yan, J. Yao, Y. S. Zhao, *Adv. Mater.* **2021**, *33*, 2104418.
[5] T. Zhang, Z. Zhou, X. Liu, K. Wang, Y. Fan, C. Zhang, J. Yao, Y. Yan, Y. S. Zhao, *J. Am. Chem. Soc.* **2021**, *143*, 20249.
[6] K. Wang, Y. Du, J. Liang, J. Zhao, F. F. Xu, X. Liu, C. Zhang, Y. Yan, Y. S. Zhao, *Adv. Mater.* **2020**, *32*, 2001999.
[7] J. Liang, M. Chu, Z. Zhou, Y. Yan, Y. S. Zhao, *Nano Lett.* **2020**, *20*, 7116.
[8] W. S. Li, W. Mi, L. J. Chen, *Displays* **2024**, *82*, 102630.
[9] H. Nasim, Y. Jamil, *Opt. Laser Technol.* **2014**, *56*, 211.

[10] C. Zhang, H. Li, D. Liang, *Nat. Commun.* **2024**, *15*, 1105.
[11] K. Roh, *Curr. Appl. Phys.* **2023**, *54*, 5.
[12] F. Koyama, *Opt. Rev.* **2014**, *21*, 893.
[13] K. Iga, *Jpn. J. Appl. Phys.* **2018**, *57*, 08PA01.
[14] T. Hamaguchi, T. Makino, K. Hayashi, J. A. Kearns, M. Ohara, M. Ito, N. Kobayashi, S. Nagane, K. Sato, Y. Nakamura, Y. Hoshina, T. Jyoukawa, T. Watanabe, Y. Kikuchi, E. Nakayama, R. Koda, N. Futagawa, *Sci. Rep.* **2022**, *12*, 21629.
[15] T. Hamaguchi, M. Tanaka, H. Nakajima, *Jpn. J. Appl. Phys.* **2019**, *58*, SC0806.
[16] M. Kuramoto, S. Kobayashi, T. Akagi, K. Tazawa, K. Tanaka, K. Nakata, T. Saito, *APEX* **2019**, *12*, 091004.
[17] F. F. Xu, Y. J. Li, Y. C. Lv, H. Y. Dong, X. Q. Lin, K. Wang, J. N. Yao, Y. S. Zhao, *CCS Chem* **2020**, *2*, 369.
[18] Y. Hou, Z. H. Zhou, C. H. Zhang, J. Tang, Y. Q. Fan, F. F. Xu, Y. S. Zhao, *Sci. China Mater.* **2021**, *64*, 2805.
[19] J. Zhao, Y. Yan, Z. Gao, Y. Du, H. Dong, J. Yao, Y. S. Zhao, *Nat. Commun.* **2019**, *10*, 870.
[20] M. Aas, A. Jonas, A. Kiraz, O. Brzobohaty, J. Jezek, Z. Pilat, P. Zemanek, *Opt. Express* **2013**, *21*, 21380.
[21] H. Yamagishi, K. Fujita, J. Miyagawa, Y. Mikami, H. Yoshioka, Y. Oki, N. Takada, S. Baba, S. Saito, S. Someya, Z. H. Lin, J. S. Huang, Y. Yamamoto, *Laser Photon. Rev.* **2023**, *17*, 2200874.
[22] N. Bentenitis, S. Krause, *Langmuir* **2005**, *21*, 6194.
[23] J. Zhang, J. D. Zahn, H. Lin, *Phys. Rev. E Stat. Nonlin. Soft Matter Phys.* **2013**, *87*, 043008.
[24] G. F. R. S. Taylor, *Proc. Math. Phys. Eng. Sci.* **1965**, *280*, 383.
[25] D. Das, D. Saintillan, *J. Fluid Mech.* **2017**, *829*, 127.
[26] S. Baba, K. Sawada, K. Tanaka, A. Okamoto, *Langmuir* **2020**, *36*, 10033.
[27] J. Klomfar, M. Součková, J. Pátek, *J. Chem. Thermodyn.* **2010**, *42*, 323.
[28] N. Tanji, J. Miyagawa, Y. Yamamoto, T. Nakashima, H. Yamagishi, *Chem. Lett.* **2023**, *52*, 696.
[29] S. Stallinga, J. M. A. van den Eerenbeemd, J. A. M. M. van Haaren, *Jpn. J. Appl. Phys.* **1998**, *37*, 560.
[30] M. Yang, I. S. Park, T. Yasuda, *J. Am. Chem. Soc.* **2020**, *142*, 19468.
[31] R. Zhu, Z. Luo, H. Chen, Y. Dong, S. T. Wu, *Opt. Express* **2015**, *23*, 23680.
[32] S. C. Yorulmaz, M. Mestre, M. Muradoglu, B. E. Alaca, A. Kiraz, *Opt. Commun.* **2009**, *282*, 3024.
[33] H. H. Yu, C. H. Yi, C. M. Kim, *Opt. Express* **2015**, *23*, 11054.
[34] J. U. Nockel, A. D. Stone, *Nature* **1997**, *385*, 45.
[35] D. Okada, Z.-H. Lin, J.-S. Huang, O. Oki, M. Morimoto, X. Liu, T. Minari, S. Ishii, T. Nagao, M. Irie, Y. Yamamoto, *Mater. Horiz.* **2020**, *7*, 1801.
[36] D. Braam, S. Kushida, R. Niemoller, G. M. Prinz, H. Saito, T. Kanbara, J. Kuwabara, Y. Yamamoto, A. Lorke, *Sci. Rep.* **2016**, *6*, 19635.
[37] R. C. Hilborn, *Am. J. Phys.* **1982**, *50*, 982.
[38] B. E. A. Saleh, M. C. Teich, *Fundamentals of Photonics*, Wiley, **2020**, 111 River Street, Hoboken, NJ 07030, USA.
[39] D. J. Bradley, *Opto-Electronics* **1974**, *6*, 25.
[40] E. G. Arthurs, D. J. Bradley, P. N. Puntambekar, I. S. Ruddock, *Opt. Commun.* **1974**, *12*, 360.
[41] O. Ostroverkhova, *Chem. Rev.* **2016**, *116*, 13279.
[42] H. Xu, L. Yin, C. Liu, X. Sheng, N. Zhao, *Adv. Mater.* **2018**, 1800156.
[43] H. Lee, Z. Jiang, T. Yokota, K. Fukuda, S. Park, T. Someya, *Mater. Sci. Eng. R Rep.* **2021**, *146*, 100631.
[44] S. Wang, J. Xu, W. Wang, G. N. Wang, R. Rastak, F. Molina-Lopez, J. W. Chung, S. Niu, V. R. Feig, J. Lopez, T. Lei, S. K. Kwon, Y. Kim, A. M. Foudeh, A. Ehrlich, A. Gasperini, Y. Yun, B. Murmann, J. B. Tok, Z. Bao, *Nature* **2018**, *555*, 83.
[45] R. Halir, P. J. Bock, P. Cheben, A. Ortega-Moñux, C. Alonso-Ramos, J. H. Schmid, J. Lapointe, D. X. Xu, J. G. Wangüemert-Pérez, I. Molina-Fernández, S. Janz, *Laser Photon. Rev.* **2015**, *9*, 25.
[46] D. M. Anderson, G. B. McFadden, A. A. Wheeler, *Annu. Rev. Fluid Mech.* **1998**, *30*, 139.
[47] N. Takada, A. Tomiyama, *JSME Int J., Ser. B* **2006**, *49*, 636.
[48] L. He, X. Huang, X. Luo, H. Yan, Y. Lü, D. Yang, Y. Han, *J. Electrost.* **2016**, *82*, 29.
[49] N. Takada, K. Mogi, T. Takaki, S. Someya, S. Baba, S. Saito, *Muntiph. Sci. Technol.* **2022**, *34*, 17.
[50] M. Shamsipur, A. A. M. Beigi, M. Teymouri, S. M. Pourmortazavi, M. Irandoust, *J. Mol. Liq.* **2010**, *157*, 43.
[51] D. Song, J. Chen, *J. Chem. Eng. Data* **2014**, *59*, 257.
[52] A. Stoppa, O. Zech, W. Kunz, R. Buchner, *J. Chem. Eng. Data* **2010**, *55*, 1768.
[53] E. L. Bennett, C. Song, Y. Huang, J. Xiao, *J. Mol. Liq.* **2019**, 294.
[54] M. Součková, J. Klomfar, J. Pátek, *Fluid Phase Equilib.* **2011**, *303*, 184.